

See discussions, stats, and author profiles for this publication at: <https://www.researchgate.net/publication/50806963>

# Theta-Shaped Plasmonic Nanostructures: Bringing “Dark” Multipole Plasmon Resonances into Action via Conductive Coupling

ARTICLE *in* NANO LETTERS · MARCH 2011

Impact Factor: 13.59 · DOI: 10.1021/nl200585b · Source: PubMed

---

CITATIONS

52

READS

86

## 5 AUTHORS, INCLUDING:



Terefe Habteyes

University of New Mexico

19 PUBLICATIONS 221 CITATIONS

[SEE PROFILE](#)



Scott Dhuey

Lawrence Berkeley National Laboratory

76 PUBLICATIONS 714 CITATIONS

[SEE PROFILE](#)



Stefano Cabrini

Lawrence Berkeley National Laboratory

213 PUBLICATIONS 2,965 CITATIONS

[SEE PROFILE](#)

# Theta-Shaped Plasmonic Nanostructures: Bringing “Dark” Multipole Plasmon Resonances into Action via Conductive Coupling

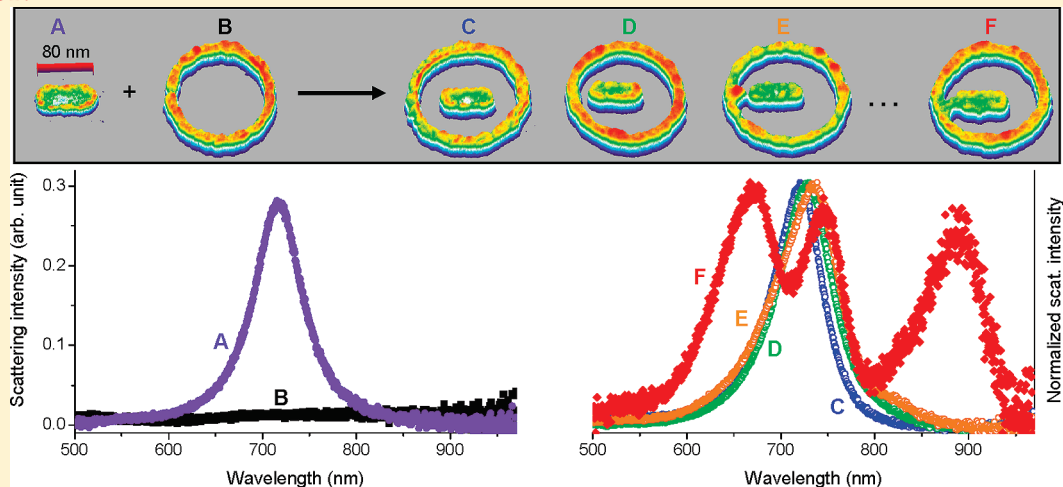
Terefe G. Habteyes,<sup>†</sup> Scott Dhuey,<sup>‡</sup> Stefano Cabrini,<sup>‡</sup> P. James Schuck,<sup>‡</sup> and Stephen R. Leone\*,<sup>†</sup>

<sup>†</sup>Departments of Chemistry and Physics, University of California, and Chemical Sciences Division, Lawrence Berkeley National Laboratory, Berkeley, California 94720, United States

<sup>‡</sup>Molecular Foundry, Lawrence Berkeley National Laboratory, Berkeley, California 94720, United States

 Supporting Information

## ABSTRACT:



Quadrupole plasmon and (octupolar) Fano resonances are induced in lithographically fabricated theta-shaped ring–rod gold nanostructures. The optical response is characterized by measuring the light scattered by individual nanostructures. When the nanorod is brought within 3 nm of the ring wall, a weak quadrupolar resonance is observed due to capacitive coupling, and when a necklike conductive bridge links the nanorod to the nanoring the optical response changes dramatically bringing the quadrupolar resonance into prominence and creating an octupolar Fano resonance. The Fano resonance is observed due to the destructive interference of the octupolar resonance with the overlapping and broadened dipolar resonance. The quadrupolar and Fano resonances are further enhanced by capacitive coupling (near-field interaction) that is favored by the theta-shaped arrangement. The interpretation of the data is supported by FDTD simulation.

**KEYWORDS:** Nanostructures, plasmon, multipole, quadrupole, octupole, Fano

Localized surface plasmon resonances are an increasingly important optical effect that have stimulated chemical and lithographic fabrications of metal nanoparticles/nanostructures with a variety of shapes including spheres,<sup>1</sup> triangles,<sup>2</sup> rods,<sup>3</sup> shells,<sup>4</sup> disks,<sup>5</sup> and rings.<sup>6</sup> In the quasi-static regime, where the size of the nanostructure is much smaller than the wavelength of the excitation light, only the plasmon mode with a dipolar charge distribution couples effectively with linearly polarized light.<sup>7–9</sup> As the size of the nanostructure increases, the electric field of the light can no longer be assumed to be uniform inside the particles, and higher order (quadrupole, octupole, etc.) plasmon modes can directly couple with the electric field of the light simply due to the phase retardation effect.<sup>7–9</sup> Excitation of multipole plasmon resonances is also caused by breaking structural symmetry, as has

been observed in gold nanoshells with an off-centered dielectric core.<sup>10</sup> For planar nanostructures that inherently support higher order modes, only the dipole plasmon resonance is excited at normal incidence, and at oblique incidence the scattering intensity of the quadrupole and octupole plasmon resonances are much weaker than that of the dipolar mode, as has been demonstrated on lithographically fabricated gold nanodisks<sup>11</sup> and nanorings.<sup>12</sup> As a result, higher order mode plasmon resonances are not easily accessible for applications of metal nanostructures such as surface enhanced spectroscopy,<sup>13</sup> solar

**Received:** February 18, 2011

**Revised:** March 13, 2011

**Published:** March 22, 2011

cell efficiency enhancement,<sup>14</sup> and molecular and biological sensors.<sup>15</sup>

It has been theoretically predicted that the quadrupole plasmon resonance of a noble metal nanoring can be excited at normal incidence through asymmetric coupling with a nanodisk.<sup>16,17</sup> The excitation of higher order modes is rationalized in terms of plasmon hybridization,<sup>18</sup> which adds a dipolar character to the multipolar modes and facilitates their coupling with the electric field of light. However, to date the excitation of higher order modes of the ring have been manifested indirectly as Fano-like interferences<sup>19</sup> when a multipolar resonance spectrally overlaps with a broad dipolar resonance.<sup>20,21</sup> For the ring multipolar mode resonances to be realized directly in the scattering spectra, the width of the ring structures needs to be scaled down,<sup>16</sup> which requires accurate fabrication techniques. In this paper, a quadrupole plasmon resonance that does not spectrally overlap with a dipolar resonance is induced in theta-shaped ring–rod gold nanostructures. In addition, a sharp Fano resonance is observed as a result of the interference between a spectrally overlapping broad dipolar resonance and a narrow octupolar resonance. The quadrupolar and Fano resonances are induced when the nanorod is displaced from the ring center and connected to the nanoring with a necklike conductive bridge. It has been reported that when nanoparticles are brought in contact, the optical response can change drastically with respect to the individual particles.<sup>22–24</sup> In the case of the ring–rod coupling presented here, the charge transfer through the conductive bridge activates the dark plasmon modes of the ring. In principle, this could also be achieved by capacitive coupling alone but the result here shows that only a weak quadrupolar resonance is observed without the conductive bridge, presumably due to plasmon losses. That is, because of the small size and roughness of the nanostructures, the plasmon energy is transferred to nonradiative processes resulting in reduced near-field amplitude.

In addition to excitation of multipole plasmon resonances, the design and fabrication of the theta-shaped plasmonic devices is motivated by the excellent individual optical properties of nanorings and nanorods. Compared to nanodisks with similar size, for example, gold nanorings have about 5 times larger refractive index sensitivities.<sup>6,25</sup> Similar to nanoshells,<sup>4</sup> the plasmon resonance energy of a nanoring is sensitively dependent on the width-to-radius aspect ratio resulting in broad optical tunability in the near-infrared region.<sup>6,25</sup> Similarly, nanorods have excellent optical tunability, large-field enhancements, and slow plasmon dephasing,<sup>26</sup> all of which are desired characteristics for optical application of metal nanostructures. The additional quadrupole plasmon resonance that is induced in the theta-shaped gold nanostructure fills the spectral gap between the dipolar resonances of the individual rod and ring.

Arrays of nanostructures, less than 200 nm in size, with 4  $\mu\text{m}$  lattice spacing are fabricated using electron-beam lithography and liftoff procedures directly on a microscope cover glass without an adhesion layer, since the adhesion layer can affect the optical response of the gold nanostructures.<sup>27</sup> A schematic of a theta-shaped ring–rod plasmonic nanostructure ( $D_{2h}$  symmetry) is shown in Figure 1a. As the rod is displaced along the laser polarization axis, the symmetry is reduced to  $C_{2v}$  and an asymmetric near-field interaction arises due to the disparity of the gaps,  $G_1 \leq G_2$ . The difference between the outer radius ( $R_2$ ) and the inner radius ( $R_1$ ) defines the width of the ring ( $\Delta R$ ), while the width and length of the rod are denoted by  $W$  and  $L$ , respectively. A representative scanning electron microscope

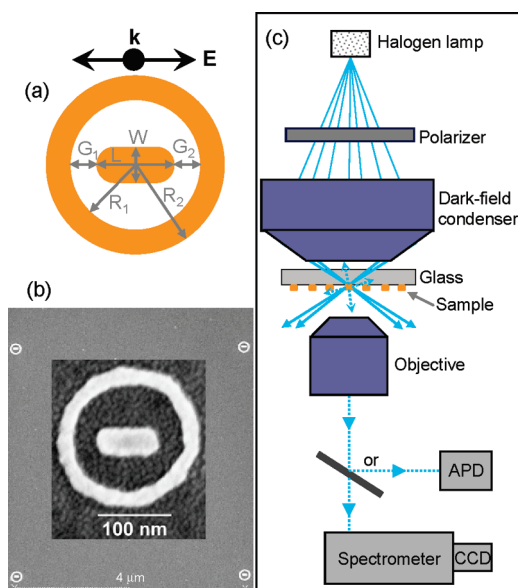


**Figure 1.** Theta-shaped ring–rod nanostructure and dark-field experimental setup. (a) Schematic of the nanostructures:  $R_1$  and  $R_2$  are the inner and outer radius of the ring, respectively;  $W$  and  $L$  are the width and length of the rod, respectively;  $G_1$  and  $G_2$  are the ring–rod gaps. The electric field ( $E$ ) is oriented along the long axis of the rod and the light propagation direction ( $k$ ) is perpendicular to the ring plane (normal incidence). (b) Representative scanning electron microscope image of portion of fabricated gold nanostructures; inset is an enlarged view of one nanostructure. (c) Schematic of scattering confocal microscope: the incident and scattered light rays are indicated by the solid and dotted cyan lines, respectively. APD is the avalanche photodiode and CCD is the charge-coupled device.

(SEM) image of fabricated structures is shown in Figure 1b. The average dimensions of the parameters are  $R_1 = 72$  nm,  $R_2 = 95$  nm,  $L = 84$  nm, and  $W = 40$  nm. The thickness (height) of the ring–rod nanostructures is  $\sim 20$  nm. Scattering spectra for individual plasmonic nanostructures are acquired using a transmission mode dark-field confocal microscope, shown in Figure 1c. The plasmonic resonances are excited by focusing white light that is polarized along the long axis of the nanorod through the back of the glass substrate using an oil immersion dark-field condenser (numerical aperture, NA = 1.2–1.4) oriented normal to the sample surface. The light scattered by an individual nanostructure is collected with a  $100\times$ , 0.95 NA air objective and spectrally analyzed by focusing through a pinhole into a spectrometer equipped with a cooled CCD camera. The  $4 \mu\text{m}$  lattice spacing and tight focusing of the excitation light ensure that the measured scattered light is due to individual nanostructures, which is important for revealing variations in the optical response resulting from slight changes in structural parameters that would otherwise be hidden by ensemble averaging.

The design of the nanostructures and the interpretation of the measured scattering spectra are facilitated by electromagnetic simulation, which is performed using the finite-difference time domain (FDTD) method and implemented with the Lumerical software package (Lumerical Solutions, Inc.). A total-field/scattered-field source scheme<sup>28</sup> is used to introduce light energy into the simulation region where the grid size is 1 nm in  $x$ -,  $y$ -, and  $z$ -directions. The bulk dielectric constants of gold measured by Johnson and Christy<sup>29</sup> are used to model the gold nanostructures. The glass substrate was included in the initial calculation

and its only effect is to red shift the resonances. Therefore, for simplicity, it is excluded in the subsequent simulations using, instead, a uniform background refractive index of 1.3. For best estimates of the actual structures, the SEM images are directly imported into the simulation region and extruded along the  $z$ -direction to define the height. That is, except for variations in height, the simulation mimics the real (fabricated) nanostructures to the accuracy of the SEM.

Representative scattering spectra corresponding to SEM images of the structures in Figure 2a are shown in Figure 2b,c. The dipolar resonance of the isolated ring lies at  $\lambda > 1000$  nm (see Supporting Information, Figure S1) and the ring quadrupolar and octupolar resonances are expected in the measured spectral window but remain dark as shown by the black line in Figure 2b. For nominally similar structures, we observe small variations in the optical response due to the slight dimensional and morphological differences. On average, with respect to that of the isolated rod (purple line) the scattering intensity increases when the rod is placed in the center of the ring (blue line). The peak wavelength and the line-width of the dipolar resonance increase monotonically as the rod is displaced from the ring center, as is evident in the spectra shown with the green and orange lines. For the spectra shown in Figure 2b, the full width at half maxima are 152 meV (rod), 155 meV (centered ring–rod), 167 meV (structure I), and 196 meV (structure II). The ring–rod gap in structure I is estimated to be  $\sim 10$  nm and no new resonances appear due to capacitive coupling. For structure II, a conductive bridge starts to form but is not complete, with a very small effective gap that is estimated to be less than 3 nm. In the corresponding spectrum (orange line), in addition to the energy shift, it can be seen that a new resonance starts to appear around the region indicated by the orange arrow. On the basis of previous theoretical predictions for silver ring–disk structures<sup>16</sup> and for gold–silica–gold nanoshells,<sup>30</sup> the spectral feature indicated by the orange arrow is attributed to the ring quadrupolar resonance that is induced as a result of capacitive coupling (near-field interaction) with the rod dipolar mode.

When the conductive bridge is completely formed, the optical response changes dramatically as shown in Figure 2c. The dipolar resonance of the rod is transformed to a highly broadened so-called superradiant mode<sup>21</sup> owing to strong hybridization with the modes of the ring. The overall width of the broad resonance indicated by the dotted horizontal arrow in Figure 2c is  $\sim 380$  meV, compared to 152 meV for the rod dipolar resonance in Figure 2b. A new prominent resonance peak with line-width of  $\sim 130$  meV appears at  $\sim 890$  nm. In addition, a spectral dip (with line-width less than 100 meV) is created at  $\sim 710$  nm on the top of the broadened dipolar resonance. The calculated scattering cross-section shown by the red line in Figure 2d agrees well with the experimental result. Although the calculated spectrum is shifted slightly to the blue, the energy separation between the observed 890 nm and 710 nm (0.35 eV) resonances is equal to the corresponding separation in the calculated spectra. The apparent difference in the relative intensity of peaks between the experimental and the calculated spectra is due to the reduced efficiency of the detector in the near-infrared region. To assist the plasmon mode assignments of the resonances, the charge distribution on the top surface is calculated at the wavelengths corresponding to the new resonances, and the results are shown in the insets in Figure 2d. The charge distributions plots clearly indicate that the resonances at  $\sim 890$  nm and 710 nm have quadrupolar ( $\ell = 2$ ) and octupolar ( $\ell = 3$ ) charge distributions with respect to the

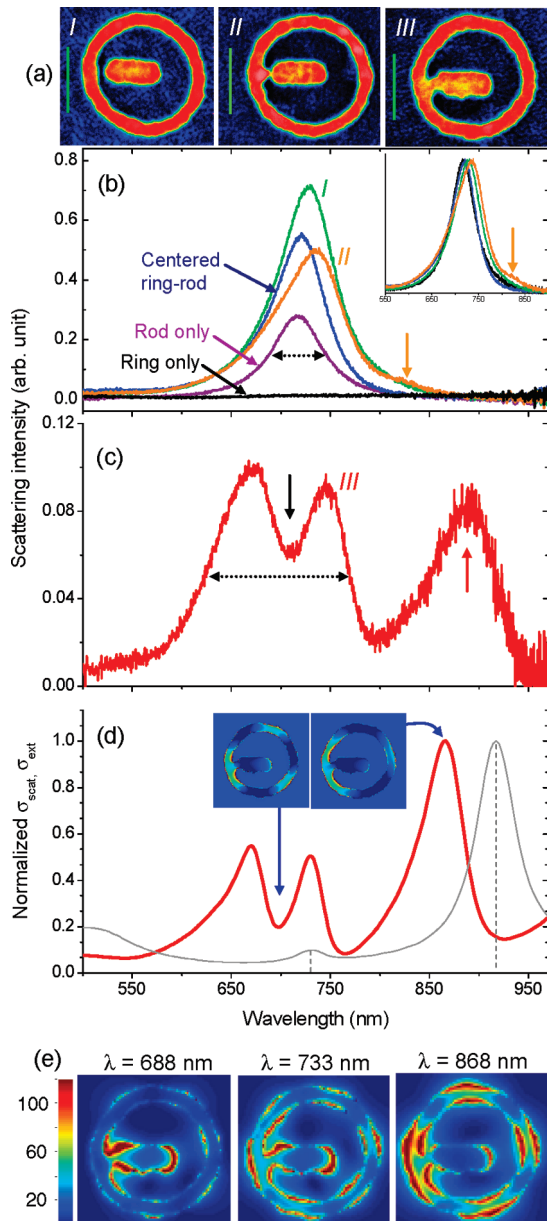


**Figure 2.** Evolution of the optical response as the nanorod is displaced from the ring center and conductively linked to the ring wall. (a) Representative SEM images of gold nanostructures (scale bar = 100 nm). (b) No resonances observed for the isolated ring (black line), and the dipolar resonance of the rod shifts to the longer wavelength as the ring–rod gap decreases. The normalized spectra are shown in the inset. The orange arrow points to a new resonance feature that starts to appear in structure II. (c) The scattering spectrum of structure III where the nanorod is conductively linked to the ring wall. The black and red arrows at 710 nm and 890 nm indicate the (octupolar) Fano and quadrupolar resonances, respectively. (d) The scattering cross-section ( $\sigma_{\text{scat}}$ , red line) of structure III calculated at normal incidence and the calculated extinction cross-section ( $\sigma_{\text{ext}}$ , gray line) of the isolated ring calculated at grazing incidence. The gray dashed vertical lines at 917 nm and 731 nm indicate the positions of quadrupolar and octupolar resonance peaks, respectively, of the isolated ring (note:  $\sigma_{\text{ext}} = \sigma_{\text{scat}} + \sigma_{\text{absorption}}$ ; the octupolar peak is not observable when  $\sigma_{\text{scat}}$  is plotted). Insets are surface charge distribution plots at the top surface. (e) Near-field intensity calculated 1 nm above the surface. The double-headed dotted horizontal arrows in (b) and (c) indicate the widths of the corresponding resonances.

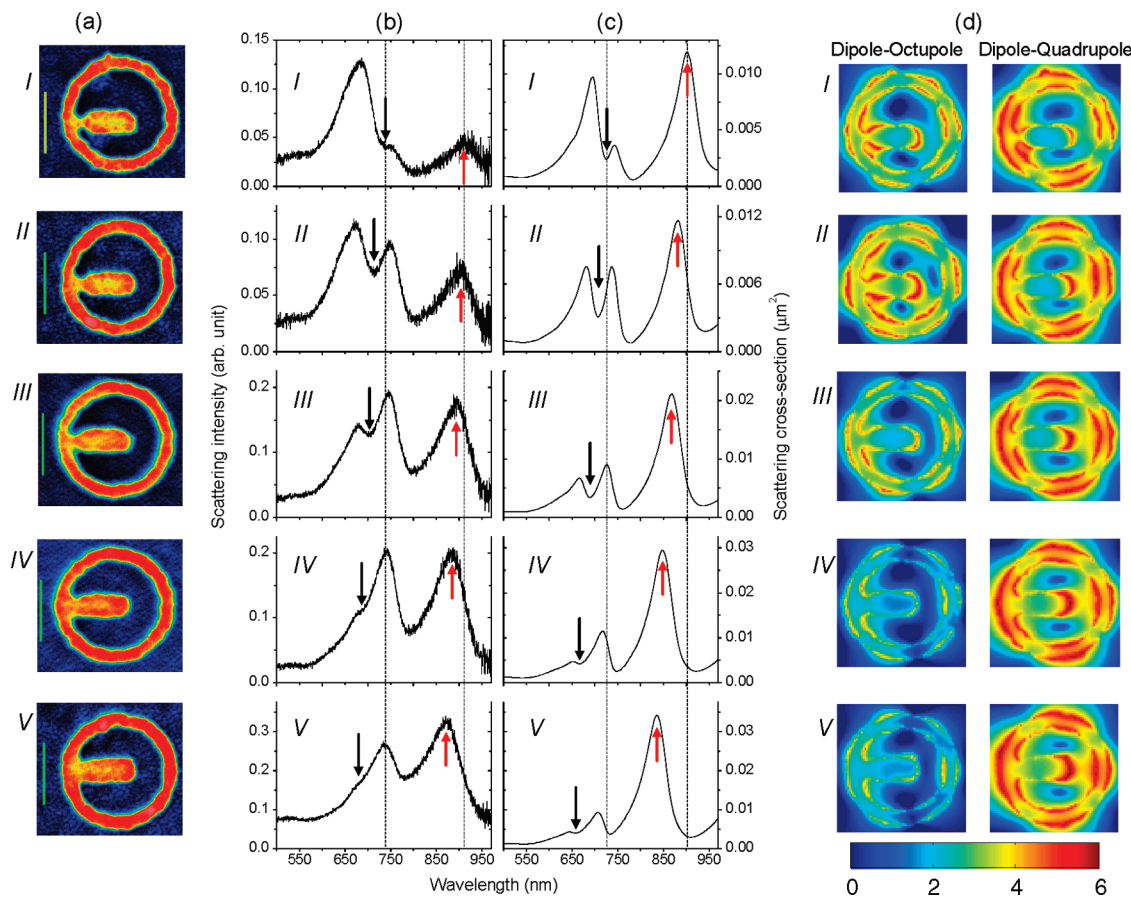


**Figure 3.** Structural sensitivity of the quadrupolar and Fano resonances. (a) The SEM images are arranged in increasing order of the bridge size (scale bar = 100 nm). Generally, the width-to-radius aspect ratio ( $\Delta R/R$ ) also increases in the same order due to fabrication properties. (b) Measured scattering spectra labeled the same as the corresponding images. (c) Calculated scattering cross-section. The red and black arrows in (c) and (d) indicate the quadrupolar and Fano resonances, respectively. The wavelength shift of the quadrupolar and Fano resonances can be seen with reference to the dotted vertical lines in (c) and (d), which show the position of the resonances for structure I. (d) The near-field intensity in natural logarithmic scale corresponding to the quadrupolar (right) and Fano (left) resonances, calculated 1 nm above the surface.

ring. In addition, the extinction cross-section of the isolated ring has been calculated at grazing incidence so that the higher order modes are excited due to retardation effects.<sup>12</sup> The normalized extinction cross-section of the ring (gray line, calculated when the incident light is propagating parallel to the ring plane) is superimposed with the scattering cross-section of the bridged ring–rod structure (red line, calculated at normal incidence) as shown in Figure 2d. As can be seen in the figure, the quadrupolar and octupolar resonances of the isolated ring appear on the longer wavelength side of the resonances observed in the bridged ring–rod structure. The energy separation between the quadrupolar and the octupolar resonance peaks of the isolated ring is 0.34 eV, which is in close agreement with the separation mentioned above. Therefore, both the surface charge plot and the correspondence with the resonances of the isolated ring suggest that the resonances at 890 nm and 710 nm are characteristic of the quadrupolar and octupolar resonances, respectively, of the ring. The octupolar resonance is manifested as a dip due to the destructive interference with the broadened dipolar resonance. This type of interference feature, referred to as a Fano resonance, has further stimulated research in plasmonics in recent years<sup>19–21,31–33</sup> (see ref 34 for review). This interpretation is further supported by the near-field intensity plots displayed in Figure 2e that directly reflect the quadrupolar and octupolar field

distribution when calculated close to the corresponding resonance peaks in Figures 2c,d. The electric field is normalized by the source, and the field intensity,  $|E|^2$ , plotted in (e), has positive amplitudes corresponding to both negative (dark) and positive (red) surface charges in Figure 2d. Both the surface charge and the near-field distribution suggest that the higher-order modes of the ring are strongly hybridized with the dipolar mode of the rod. However, for brevity, the resonance at 890 nm is simply referred to as a quadrupole plasmon resonance.

The resonance energy of the multipole resonances depends very sensitively on the structural parameters, particularly the conductive bridge size and the ring width-to-radius aspect ratio ( $\Delta R/R$ ). The rod dipolar resonance, on the other hand, is less sensitive to slight structural changes. The observation of the Fano resonance mainly depends on the energy position of the ring octupolar resonance as illustrated in Figure 3. As the bridge size increases from panels I to V in Figure 3a, both the quadrupolar and the octupolar resonances shift to shorter wavelength as shown in the experimental spectra (Figure 3b), which agrees well with the calculated spectra (Figure 3c). For example, as the structural parameters change slightly from panel I to II, the octupolar resonance shifts from the right shoulder of the dipolar resonance to near degeneracy. As a result, the Fano resonance in Figures 3b,c, which is also similar to the one in Figure 2c, can be

considered as plasmon-(electromagnetic) induced transparency, which has been predicted<sup>35</sup> and observed<sup>31</sup> in metamaterials. As the bridge size further increases as in panels III and IV, the octupolar resonance shifts to the left shoulder of the dipolar resonance, and the interaction becomes weaker as reflected in the shallow depth of the Fano resonance. Finally, when the nanorod is uniformly merged to the wall of the ring the octupolar resonance disappears to the blue while the quadrupolar resonance takes precedence. In this limit, the ring–rod structure can be considered as a single nanostructure that supports four resonances corresponding to the dipolar mode of the rod and the dipolar, quadrupolar, and octupolar modes of the ring covering a spectral range from about 580 to 1400 nm.

Although it is less apparent in the SEM images shown in Figure 3a, the multipole resonances also shift to the blue with increasing  $\Delta R/R$ . In general, the fabrication process increases/decreases the sizes of the bridge and the  $\Delta R/R$  in the same direction, that is, because of the proximity of the bridge to the ring wall, the conditions that increase the conductive bridge area also increase the width of the ring and vice versa. Therefore, although it is difficult to quantify the bridge size independently, a general trend can be obtained by analyzing the spectra with respect to  $\Delta R/R$ , and the result can be compared to theory. First, to vary the structural parameters theoretically, the simulation is performed using idealized ring–rod primitive structures similar to the one in Figure 1a. The calculated spectra shown in Figures 4a,b are obtained using a 40 nm  $\times$  84 nm rod and using several ring parameters specified in the figures. In contrast to the experimental observation, the multipole resonances are induced even at a ring–rod gap of 15 nm due to capacitive coupling, blue line in Figure 4a. As the gap size decreases, the Fano resonance becomes stronger and the quadrupolar resonance shifts to the red (green and red lines). The result of the simulation is consistent with similar theoretical results reported for nonconcentric silver ring–disk nanostructures<sup>16</sup> and gold–silica–gold nanoshells.<sup>30</sup> The fact that the multipole plasmon resonances are not observed in the experimental results in Figures 2a,b even at smaller gaps is attributed to the plasmon loss most likely due to grains in the fabricated structures. However, consistent with the experimental result, when the rod uniformly merges to the ring, the resonances jump to the shorter wavelengths (gray line). To illustrate the effect of  $\Delta R/R$  computationally, the width is increased (keeping  $G_1$  and  $R_2$  constant), and the resulting spectra are plotted in Figure 4b. In Figure 4c, the resonance energies (solid lines) extracted from Figure 4b are compared with the experimental data (solid squares and solid circles). Compared to the simulation the experimental results have greater slopes, which, based on the results in Figure 3, can be attributed to the influence of the bridge size that is not accounted for in the simulation. The spectra in Figure 4b are for  $G_1 = 5$  nm; as a result, the calculated resonance energies plotted in Figure 4c are lower than the experimental values due to the capacitive coupling which decreases the resonance energy as discussed next.

Before the conductive bridge is formed, opposite charges build up on the opposite sides of the dielectric medium and a strong Coulomb attraction shifts the resonance progressively to lower energy with decreasing interparticle distance.<sup>36,37</sup> When the conductive bridge is formed, the surface charges around the interfaces are allowed to move, reducing the capacitive coupling (Coulomb attraction), and the resonances jump to higher energy.<sup>22,38,39</sup> The resonance energy further increases as the conductive bridge fills the dielectric medium, as demonstrated in

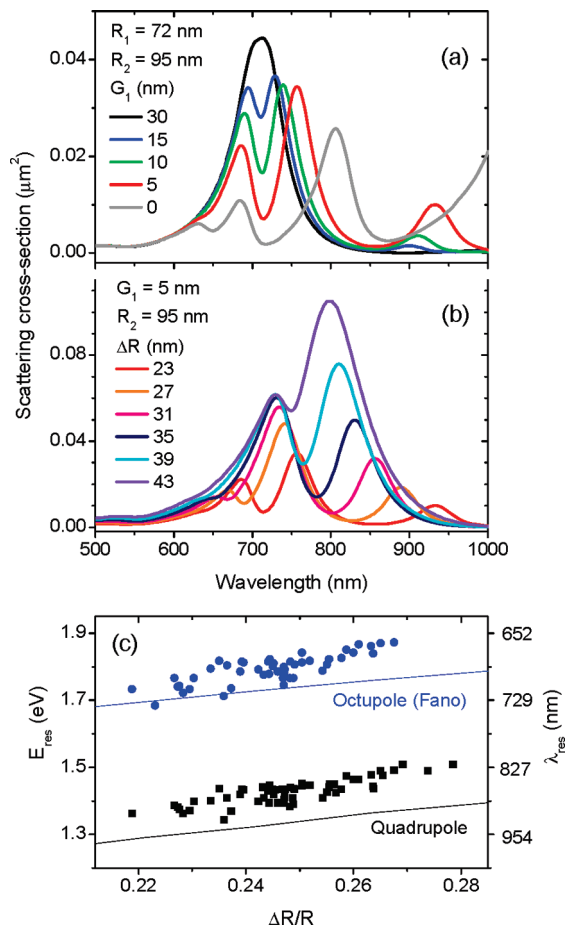


**Figure 4.** Calculated spectra of idealized structures and comparison with the experimental data. The ring and gap parameters are specified on the plot, and the rod width and length are 40 and 84 nm, respectively. Both the ring and the rod are 20 nm high. (a) The resonances shift continuously to the longer wavelength when the ring–rod gap ( $G_1$ ) is decreased by displacing the rod from the ring center (black line) along the laser polarization axis, and jumps to the shorter wavelength when the rod is merged to the ring wall (gray line). (b) The quadrupolar resonance shifts to the blue and eventually overlaps with the dipolar resonance of the rod when the  $\Delta R$  is increased at the expense of  $R_1$ . (c) The resonances extracted from (b) are plotted (solid lines) as a function of  $\Delta R/R$ , where  $R$  is chosen to be  $R_2$  and compared with the resonances obtained from experimental spectra (black filled squares and blue filled circles).

the experimental results presented in Figures 3a,b. However, because of the curvature of the ring the capacitive coupling is still prevalent even after the conductive coupling is fully established. This is evident in the near-field intensity contour plot displayed in Figure 3d where we see field localization around the bridge as displayed in panels I–III. The field is pushed out of the junction region as the conductive bridge widens and fills the dielectric medium around the neck, and it becomes stronger between the opposite end of the rod and the ring wall as in panels IV and V. Previous calculations also show that there is a uniform electric field in the area enclosed by the ring when the ring resonances are excited.<sup>6</sup> When the nanorod is linked to the ring from outside (see Supporting Information, Figure S2), as reported for a gold ring–disk system,<sup>20</sup> the resonances shift to the blue compared to the corresponding resonances when the nanorod is inside the

ring, indicating reduced near-field interaction. In addition, the scattering and absorption cross-section and the near-field amplitudes significantly decrease for the outside coupling case. Therefore, in the theta-shaped structure both conductive and capacitive coupling contribute to the ring–rod plasmon interaction, and the mechanism of the interaction can be summarized as follows. The electric field of the light excites a dipolar charge oscillation in the nanorod and the flow of an oscillating electrical current through the conductive bridge induces the quadrupolar and octupolar resonances that do not directly couple to the light. The Fano resonance is created when the less radiative sharp octupolar resonance destructively interferes with the radiative broadened dipolar resonance. The capacitive coupling further increases the interaction leading to strong quadrupolar and Fano resonances. For the small ring sizes considered here, the multipolar resonances are not induced effectively by near-field coupling owing to the plasmon damping via nonradiative processes. The uneven (noncrystalline) structures further facilitate the loss. The flow of oscillating current through the conductive bridge effectively activates the higher-order charge oscillation modes in the entire ring, bringing the “dark” multipole plasmon modes into action. More intuitive understanding can be obtained by representing the conductive bridge, the nanorod, and the nanoring as circuit nanoelements,<sup>40</sup> which can be a focus of future work.

In summary, quadrupole plasmon and (octupolar) Fano resonances are induced in conductively coupled theta-shaped ring–rod gold nanostructures. Because of the wide spectral coverage from about 600 nm to 1400 nm with sharp resonance features, these nanostructures can potentially be used as universal plasmonic devices in various optical applications such as surface-enhanced spectroscopy and plasmon sensors. In addition, the experimental results provide evidence that conductive coupling mechanisms can bring interesting plasmon resonances into effect that otherwise are not possible, paving the way for improved design of plasmonic devices.

## ■ ASSOCIATED CONTENT

**Supporting Information.** Additional simulation results are provided. This material is available free of charge via the Internet at <http://pubs.acs.org>.

## ■ AUTHOR INFORMATION

### Corresponding Author

\*E-mail: srl@berkeley.edu.

## ■ ACKNOWLEDGMENT

T.G.H. is supported by the University of California President's Postdoctoral Fellowship Program. Supplies and equipment are provided through the Materials Research Division (MSD), Lawrence Berkeley National Laboratory (LBNL), and the nano-fabrication and optical measurements were performed as a User project at the Molecular Foundry, LBNL. The funds through the MSD and the work at the Molecular Foundry are supported by the Office of Science, Office of Basic Energy Sciences, of the U.S. Department of Energy under Contract No. DE-AC02-05CH11231.

## ■ REFERENCES

- (1) Jana, N. R.; Gearheart, L.; Murphy, C. J. *Langmuir* **2001**, *17* (22), 6782–6786.
- (2) Zhang, Z.; Weber-Bargioni, A.; Wu, S. W.; Dhuey, S.; Cabrini, S.; Schuck, P. J. *Nano Lett.* **2009**, *9* (12), 4505–4509.
- (3) Nikoobakht, B.; El-Sayed, M. A. *Chem. Mater.* **2003**, *15* (10), 1957–1962.
- (4) Oldenburg, S. J.; Averitt, R. D.; Westcott, S. L.; Halas, N. J. *J. Chem. Phys. Lett.* **1998**, *288* (2–4), 243–247.
- (5) Hanarp, P.; Kall, M.; Sutherland, D. S. *J. Phys. Chem. B* **2003**, *107* (24), 5768–5772.
- (6) Aizpurua, J.; Hanarp, P.; Sutherland, D. S.; Kall, M.; Bryant, G. W.; de Abajo, F. J. *G. Phys. Rev. Lett.* **2003**, *90* (5), 4.
- (7) Kelly, K. L.; Coronado, E.; Zhao, L. L.; Schatz, G. C. *J. Phys. Chem. B* **2003**, *107* (3), 668–677.
- (8) Bohren, C. F.; Huffman, D. R. *Absorption and Scattering of Light by Small Particles*; Wiley-VCH: Weinheim, 2004.
- (9) Kreibig, U.; Vollmer, M. *Optical Properties of Metal Clusters*; Springer: Berlin, 1995.
- (10) Wang, H.; Wu, Y. P.; Lassiter, B.; Nehl, C. L.; Hafner, J. H.; Nordlander, P.; Halas, N. J. *Proc. Natl. Acad. Sci. U.S.A.* **2006**, *103* (29), 10856–10860.
- (11) Esteban, R.; Vogelgesang, R.; Dorfmuller, J.; Dmitriev, A.; Rockstuhl, C.; Etrich, C.; Kern, K. *Nano Lett.* **2008**, *8* (10), 3155–3159.
- (12) Hao, F.; Larsson, E. M.; Ali, T. A.; Sutherland, D. S.; Nordlander, P. *Chem. Phys. Lett.* **2008**, *458* (4–6), 262–266.
- (13) Moskovits, M. *Rev. Mod. Phys.* **1985**, *57* (3), 783–826.
- (14) Nakayama, K.; Tanabe, K.; Atwater, H. A. *Appl. Phys. Lett.* **2008**, *93* (12), 3.
- (15) Elghanian, R.; Storhoff, J. J.; Mucic, R. C.; Letsinger, R. L.; Mirkin, C. A. *Science* **1997**, *277* (5329), 1078–1081.
- (16) Hao, F.; Sonnenaud, Y.; Van Dorpe, P.; Maier, S. A.; Halas, N. J.; Nordlander, P. *Nano Lett.* **2008**, *8* (11), 3983–3988.
- (17) Hao, F.; Nordlander, P.; Sonnenaud, Y.; Van Dorpe, P.; Maier, S. A. *ACS Nano* **2009**, *3* (3), 643–652.
- (18) Prodan, E.; Radloff, C.; Halas, N. J.; Nordlander, P. *Science* **2003**, *302* (5644), 419–422.
- (19) Christ, A.; Ekinci, Y.; Solak, H. H.; Gippius, N. A.; Tikhodeev, S. G.; Martin, O. J. *F. Phys. Rev. B* **2007**, *76* (20), 4.
- (20) Verellen, N.; Sonnenaud, Y.; Sobhani, H.; Hao, F.; Moshchalkov, V. V.; Van Dorpe, P.; Nordlander, P.; Maier, S. A. *Nano Lett.* **2009**, *9* (4), 1663–1667.
- (21) Sonnenaud, Y.; Verellen, N.; Sobhani, H.; Vandenbosch, G. A. E.; Moshchalkov, V. V.; Van Dorpe, P.; Nordlander, P.; Maier, S. A. *ACS Nano* **2010**, *4* (3), 1664–1670.
- (22) Atay, T.; Song, J. H.; Nurmiikko, A. V. *Nano Lett.* **2004**, *4* (9), 1627–1631.
- (23) Danckwerts, M.; Novotny, L. *Phys. Rev. Lett.* **2007**, *98* (2), 4.
- (24) Lassiter, J. B.; Aizpurua, J.; Hernandez, L. I.; Brandl, D. W.; Romero, I.; Lal, S.; Hafner, J. H.; Nordlander, P.; Halas, N. J. *Nano Lett.* **2008**, *8* (4), 1212–1218.
- (25) Larsson, E. M.; Alegret, J.; Kall, M.; Sutherland, D. S. *Nano Lett.* **2007**, *7* (5), 1256–1263.
- (26) Sonnichsen, C.; Franzl, T.; Wilk, T.; von Plessen, G.; Feldmann, J.; Wilson, O.; Mulvaney, P. *Phys. Rev. Lett.* **2002**, *88* (7), 4.
- (27) Lahiri, B.; Dylewicz, R.; De la Rue, R. M.; Johnson, N. P. *Opt. Express* **2010**, *18* (11), 11202–11208.
- (28) Taflove, A.; Hagness, S. C. *Computational Electrodynamics The Finite-Difference Time-Domain Method*; Artech House: Boston, 2005.
- (29) Johnson, P. B.; Christy, R. W. *Phys. Rev. B* **1972**, *6* (12), 4370–4379.
- (30) Hu, Y.; Noelck, S. J.; Drezek, R. A. *ACS Nano* **2010**, *4* (3), 1521–1528.
- (31) Liu, N.; Langguth, L.; Weiss, T.; Kastel, J.; Fleischhauer, M.; Pfau, T.; Giessen, H. *Nat. Mater.* **2009**, *8* (9), 758–762.
- (32) Fan, J. A.; Wu, C. H.; Bao, K.; Bao, J. M.; Bardhan, R.; Halas, N. J.; Manoharan, V. N.; Nordlander, P.; Shvets, G.; Capasso, F. *Science* **2010**, *328* (5982), 1135–1138.
- (33) Hentschel, M.; Saliba, M.; Vogelgesang, R.; Giessen, H.; Alivisatos, A. P.; Liu, N. *Nano Lett.* **2010**, *10* (7), 2721–2726.

- (34) Luk'yanchuk, B.; Zheludev, N. I.; Maier, S. A.; Halas, N. J.; Nordlander, P.; Giessen, H.; Chong, C. T. *Nat. Mater.* **2010**, *9* (9), 707–715.
- (35) Zhang, S.; Genov, D. A.; Wang, Y.; Liu, M.; Zhang, X. *Phys. Rev. Lett.* **2008**, *101* (4), 4.
- (36) Rechberger, W.; Hohenau, A.; Leitner, A.; Krenn, J. R.; Lamprecht, B.; Aussenegg, F. R. *Opt. Commun.* **2003**, *220* (1–3), 137–141.
- (37) Su, K. H.; Wei, Q. H.; Zhang, X.; Mock, J. J.; Smith, D. R.; Schultz, S. *Nano Lett.* **2003**, *3* (8), 1087–1090.
- (38) Romero, I.; Aizpurua, J.; Bryant, G. W.; de Abajo, F. J. G. *Opt. Express* **2006**, *14* (21), 9988–9999.
- (39) Perez-Gonzalez, O.; Zabala, N.; Borisov, A. G.; Halas, N. J.; Nordlander, P.; Aizpurua, J. *Nano Lett.* **2010**, *10* (8), 3090–3095.
- (40) Engheta, N.; Salandrino, A.; Alu, A. *Phys. Rev. Lett.* **2005**, *95* (9), 4.